XL CILAMCE
IBERO-LATIN AMERICAN CONGRESS ON COMPUTATIONAL METHODS IN ENGINEERING
NOVEMBER 11-14, 2019
Praiamar Natal Hotel & Convention
Natal, RN-BRAZIL

COUNTERINTUITIVE PHYSICAL BEHAVIORS IN COUPLED CONSOLIDATION PROBLEMS

Hermínio T. Honório
Aideé A. Torres
Bruno Martins
Carlos A. S. Ferreira
Felipe W. Giacomelli
Clovis R. Maliska
herminio@sinmec.ufsc.br
aideetorres@sinmec.ufsc.br
bmartins@sinmec.ufsc.br
casf@sinmec.ufsc.br
fe.wallner@gmail.com
maliska@sinmec.ufsc.br
Department of Mechanical Engineering - Federal University of Santa Catarina
Campus Universitário, 88.040-900, Santa Catarina, Brasil

Abstract. The coupled nature of the equations composing Biot's consolidation model often produces quite unexpected behaviors. The most common one is the Mandel-Cryer effect, which refers to a pressure increase in certain regions of the domain for a short period of time with no apparent reason. Although this effect is well known and widely reported in the literature, a clear and comprehensive explanation on the physical mechanism that causes of the Mandel-Cryer effect is not easily found. Another counterintuitive behavior is observed in a fully saturated poroelastic column under the influence of a gravitational field. In this case, the poroelastic properties can produce displacement profiles that defies the common sense. In this paper, we provide a deep discussion on these phenomena and a few hypotheses for explaining them are proposed. For instance, we argue that there must be a mechanism responsible for transferring volumetric strain to different regions of the domain in order to occur the Mandel-Cryer effect. For the poroelastic column, we propose a spring-mass system to explain the displacement profiles obtained in different situations. All of these hypotheses are carefully tested through numerical experiments.

Keywords: Poroelasticity, Biot's consolidation model, coupled consolidation, Mandel-Cryer effect, poroelastic column

1 Introduction

The first theoretical analysis of a 1-D consolidation column undergoing an external compressive load was first developed by Terzaghi [1, 2]. Later on, Biot generalized this theory to three dimensions [3] and for anisotropic materials [4], and since then, it has been referred to as Biot's theory of consolidation. Consolidation processes are generally coupled with the fluid flow in porous media, since the fluid flow through the pore channels affects the pore pressure field, which causes a force imbalance in the solid matrix. As a result, the porous matrix deforms in order to reach a new equilibrium state. The solid deformation directly changes pressure field and thus the fluid flow. The coupling between these two processes are mathematically described by Biot's consolidation model.

Although consolidation processes are well understood, the coupling nature of this phenomenon often produces quite weird effects that goes in opposite direction of common sense. A classical example is the Mandel-Cryer effect [5, 6], which predicts an apparently unphysical pressure increase in specific regions of the domain for a short period of time. The classical problems where this effect can be observed are the Mandel's problem [5] and the Cryer's sphere [6], for which analytical solutions are available. The Mandel-Cryer effect is predicted not just by the analytical solutions but also by numerical solutions. In fact, these two problems are widely used in the literature for verifying numerical schemes for solving coupled poroelasticity problems. Beyond these classical problems, the Mandel-Cryer effect has been first observed in a real situation in a small village called Noordbergum, in the Netherlands, when a pressure increase has been detected in the upper layer of an aquifer during groundwater withdrawal. Since then, it has been known as the Noordbergum effect [7–9]. Furthermore, this effect has been captured by a numerical experiment setup by Dean et al. [10] where a pay region (reservoir) with a production well at its center is surrounded by a nonpay region. When the well starts the production, a pressure increase is detected near the boundaries of the pay region, which is a clear indication of the Mandel-Cryer effect. Although it is widely reported in the literature, a clear and detailed explanation on the physics behind this phenomenon is not easily found anywhere.

Aside from the Mandel-Cryer effect, there is another quite unexpected behavior that appears in a fully sealed poroelastic column subjected to oedometric conditions and under the influence of the gravitational field. In this case, it would be natural to expect the vertical displacement profile to monotonically vary from zero at the bottom to its maximum value at the upper boundary, which is precisely what happens for a solid material. However, for a nearly incompressible fluid and a very soft material, the vertical displacement profile presents its maximum value somewhere in the middle of the column, which is a quite uncomfortable behavior at first glance. In this problem, the fluid density also plays an interesting role in the behavior of the equilibrium state (displacement profile), as it can exert a force at the upper boundary of the column. To the knowledge of the authors, a deep discussion on the causes of this behavior is not reported in the literature.

This paper presents a careful discussion on these counterintuitive behaviors originated from coupled poroelasticity. Special emphasis is given to the physical processes involved and on the role played by the poromechanical properties. The rationale in this paper is to discuss the physics behind coupled consolidation, analyze the model equations, provide hypotheses to explain these unexpected phenomena and test them through numerical experiments. First, the Mandel-Cryer effect is discussed and a hypothesis is developed to explain how it operates. In the sequence, the poroelastic column immersed in the gravitational field is described and a spring-mass system is proposed to explain the different situations that can occur. Finally, a set of numerical experiments are performed in order to reproduce the physical effects and to test the hypotheses previously proposed. Finally, a few remarks close the presentation.

2 Governing equations

Biot's theory of consolidation is described by mass and momentum conservation equations. In this case, the momentum equations, often referred to as equilibrium equations, consider the effective stress principle of Terzaghi [1, 2] in order to account for the influence of the pore pressure p, which leads to

the following equation,

$$\nabla \cdot (\boldsymbol{\sigma}' - \alpha p \mathbf{I}) + \rho \mathbf{g} = 0, \tag{1}$$

where $\mathbf{I}$ is a second order identity tensor, $\mathbf{g}$ is the gravitational acceleration vector, ρ is a porosity weighted density of solid (ρ_s) and fluid (ρ_f) phases, that is, $\rho = \phi\rho_f + (1-\phi)\rho_s$, with ϕ representing porosity. Finally, the effective stress tensor acting on the solid matrix, for linear elasticity is given by

$$\sigma'_{ij} = 2G\epsilon_{ij} + \lambda\epsilon_{kk}\delta_{ij}, \tag{2}$$

with G being the shear modulus, λ the first Lamé's parameter and ϵ_{ij} the components of the strain tensor $\boldsymbol{\epsilon}$. By assuming small strains, the strain tensor relates to the displacement vector $\mathbf{u}$ as follows,

$$\boldsymbol{\epsilon} = \frac{1}{2}(\nabla \mathbf{u} + \nabla \mathbf{u}^T). \tag{3}$$

Usually, the mass balance equation for fluid flow in porous media only considers fluid phase velocity. However, for deformable porous media the solid motion (solid velocity, $\mathbf{v}_s$) also has to be taken into account since the pore channels in the solid matrix transports fluid as it deforms. According to Biot's theory of consolidation, the mass balance equation for fluid flow in deforming porous media can be represented as

$$\frac{1}{Q}\frac{\partial p}{\partial t} + \nabla \cdot (\mathbf{v} + \alpha \mathbf{v}_s) = 0, \tag{4}$$

where the Biot modulus [11] is $1/Q = c_f\phi + (\alpha - \phi)c_s$, with α being Biot-Willis coefficient [12] and c_f and c_s are the fluid and solid phase compressibilities, respectively. Still on Eq. (4), p is the fluid pore pressure, $\mathbf{v}_s$ is the solid velocity, given by the time derivative of the displacement vector $\mathbf{u}$, and $\mathbf{v}$ is the relative fluid phase velocity, represented by Darcy's law, that is,

$$\mathbf{v} = -\frac{\mathbf{k}}{\mu} \cdot (\nabla p - \rho_f \mathbf{g}), \tag{5}$$

with μ begin the fluid viscosity and $\mathbf{k}$ the absolute permeability tensor.

By recognizing that the volumetric strain is given by $\epsilon_v = \nabla \cdot \mathbf{u}$ and assuming α to be independent of the position $\mathbf{r}$, Eq. (4) can be written in a more usual form,

$$\frac{1}{Q}\frac{\partial p}{\partial t} + \nabla \cdot \mathbf{v} = -\alpha \frac{\partial \epsilon_v}{\partial t}. \tag{6}$$

For closuring the model equations, the initial and boundary conditions must be specified. The domain occupied by the porous medium can be denoted by Ω and it is bounded by a surface Γ. In addition, let $\hat{\mathbf{n}}$ be a unitary normal vector defined over the boundary Γ and pointing outwards the domain Ω. The surface boundary can be divided into regions subjected to Dirichlet boundary conditions, denoted by Γ_D^p and $\Gamma_D^{\mathbf{u}}$ for $\mathbf{u}$ and p, respectively, and to Neumann boundary conditions, denoted by Γ_N^p and $\Gamma_N^{\mathbf{u}}$, respectively, such that $\Gamma_D^p \cap \Gamma_N^p = \emptyset$ and $\Gamma_D^{\mathbf{u}} \cap \Gamma_N^{\mathbf{u}} = \emptyset$. These sets are represented in Fig. 1.

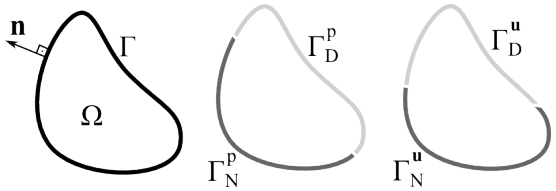

Figure 1. Domain Ω and boundary sets.

Finally, the problem can be stated as finding $p = p(\mathbf{r}, t)$ and $\mathbf{u} = \mathbf{u}(\mathbf{r}, t)$ such that,

$$\nabla \cdot (\boldsymbol{\sigma}' - \alpha p \mathbf{I}) + \rho \mathbf{g} = 0 \quad \forall \ \mathbf{r} \in \Omega \tag{7}$$

$$\frac{1}{Q}\frac{\partial p}{\partial t} + \nabla \cdot \mathbf{v} = -\alpha \frac{\partial \epsilon_v}{\partial t} \quad \forall \ \mathbf{r} \in \Omega \tag{8}$$

$$\mathbf{v} = -\frac{\mathbf{k}}{\mu} \cdot (\nabla p - \rho_f \mathbf{g}) \quad \forall \ \mathbf{r} \in \Omega \tag{9}$$

$$(\boldsymbol{\sigma}' + \alpha p \mathbf{I}) \cdot \hat{\mathbf{n}} = \mathbf{t} \quad \forall \ \mathbf{r} \in \Gamma_N^u \tag{10}$$

$$\mathbf{u} = \bar{\mathbf{u}} \quad \forall \ \mathbf{r} \in \Gamma_D^u \tag{11}$$

$$-\mathbf{v} \cdot \hat{\mathbf{n}} = \dot{\omega} \quad \forall \ \mathbf{r} \in \Gamma_N^p \tag{12}$$

$$p = \bar{p} \quad \forall \ \mathbf{r} \in \Gamma_D^p \tag{13}$$

$$p(\mathbf{r}, 0) = p_0 \quad \forall \ \mathbf{r} \in \Omega \tag{14}$$

$$\mathbf{u}(\mathbf{r}, 0) = \mathbf{u}_0 \quad \forall \ \mathbf{r} \in \Omega \tag{15}$$

where $\mathbf{t}$ is the traction vector, $\bar{\mathbf{u}}$ and $\bar{p}$ are the prescribed displacement vector and pressure, $\dot{\omega}$ is the volumetric flux, and the pressure and displacement fields at time $t = 0$ are denoted by p_0 and $\mathbf{u}_0$, respectively.

3 The Mandel-Cryer effect

One of the key points to understand the Mandel-Cryer effect is the interplay between the volumetric strain and the pore pressure. This means to understand how a pressure change affects the volumetric strain and vice-versa. Another crucial ingredient for the Mandel-Cryer effect to happen is a special setup of the boundary conditions in which a contraction (or expansion) in one region causes a contraction (or expansion) in another region of the domain, where a pressure increase (or decrease) is observed. Therefore, the Mandel-Cryer effect is a combination of this mechanism that transfers a contraction (or expansion) from one place to another with the relationship between the pore pressure and volumetric strain. These two points are discussed below.

3.1 Volumetric strain and pore pressure

Understanding the relationship between pore pressure and volumetric strain in the solid matrix is key for understanding the Mandel-Cryer effect. It is quite intuitive that when the pore pressure increases, the porous matrix tends to expand, that is, to increase its volume. Conversely, if a pressure decrease is experienced by the fluid filling the pore channels, it tends to pull the solid grains together thus reducing the bulk volume. In the same manner, if an external load forces the porous matrix to shrink, the pore pressure will instantly increase before it starts to dissipate as the fluid starts to migrate to low pressure regions. The opposite behavior should be observed if the external load imposes an expansion to the porous matrix. This phenomenon is totally equivalent to material dilation, which is the mechanical response of material due to temperature changes. In fact, the mathematical formulation of both poroelasticity and termoelasticity are quite the same.

Mathematically, the interplay between pore pressure and volumetric strain can be disclosed by performing a time integration of Eq. (6)between time t and $t + \Delta t$, which leads to,

$$p^{t+\Delta t} = p^t - \alpha Q(\epsilon_v^{t+\Delta t} - \epsilon_v^t) - Q \int_t^{t+\Delta t} \nabla \cdot \mathbf{v} \mathrm{dt} \tag{16}$$

or,

$$\epsilon_v^{t+\Delta t} = \epsilon_v^t - \frac{(p^{t+\Delta t} - p^t)}{\alpha Q} - \frac{1}{\alpha} \int_t^{t+\Delta t} \nabla \cdot \mathbf{v} \mathrm{dt} \tag{17}$$

The integrals on the RHS of Equations 16 and 17 are responsible for alleviating pressure as time progresses. Thus any pressure increase caused by a contraction of the porous matrix tends to vanish as the fluid flows towards low pressure regions, according to Darcy's law, in order to equalize the pressure field.

Furthermore, for the sake of simplicity, if we consider $p^t = \epsilon_v^t = 0$ and a very small time step size Δt so the fluid does not have enough time to move through the pore channels (undrained consolidation), then the relationship between the pore pressure and volumetric strain becomes

$$p^{t+\Delta t} = -\alpha Q \epsilon_v^{t+\Delta t}, \tag{18}$$

which highlight that a negative volumetric strain (contraction) produces a positive pressure (pressure increase), and vice-versa. It is important however to keep in mind that for a drained condition, i.e. when fluid has enough time to move through the pore channels, wherever there is a pressure decrease a local negative volumetric strain is observed. In other words, wherever there is fluid loss, locally, the porous medium shrinks and the bulk volume decreases. Conversely in an undrained condition, if an external force causes a positive volumetric strain (expansion) somewhere in the porous medium, the pore pressure in that region will immediately drop and fluid will then flow towards the low pressure region to equalize the pressure levels.

3.2 Boundary conditions setup

Once the relationship between volumetric strain and pore pressure is well understood, we now investigate the particular conditions in which the Mandel-Cryer effect appears. These conditions are a sort of mechanism that transfer the volumetric strain observed in a region A of the porous material to another region B, thus affecting the pore pressure at region B. A schematic representation of this idea is depicted in Fig. 2, in which a volumetric strain $\epsilon_{v,A}$ in region A is transfered, through some mechanism, to region B, denoted by $\epsilon_{v,B}$. According to Eq. (18), at least for a short period of time, the pore pressure should be affected at region B due to $\epsilon_{v,B}$.

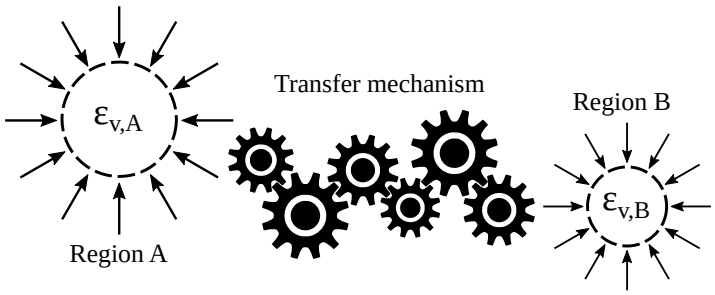

Figure 2. Schematic representation of the mechanism that transfers volumetric strain from one place to another.

Different setups of boundary conditions can create mechanisms that provide the transferring of volumetric strain from one place to another. The classical ones are the Mandel's problem and the Cryer's sphere, which are discussed below. The discussions will remain in the theoretical realm, since their purpose is to provide hypotheses to explain the Mandel-Cryer effect that will be tested in the results section.

Mandel's problem

Mandel's problem refers to a two-dimensional poroelastic slab of length $2L$ and height $2H$, as depicted in Fig. 3a. The lateral boundaries ($x = L$ and $x = -L$) are fully permeable, so the pore pressure P_{out} is prescribed (usually $P_{\text{out}} = 0$). The top and bottom boundaries are subjected to a constant force of $2F$. A very important detail in this problem is that the top and bottom boundaries are required to be

horizontal during the whole simulation, that is, the vertical displacement, v, has to be the same along these boundaries. Mathematically, this means that

$$\left.\frac{\partial v}{\partial x}\right|_{y=H} = \left.\frac{\partial v}{\partial x}\right|_{y=-H} = 0 \tag{19}$$

Finally, the initial pore pressure p^0 and volumetric strain ϵ_v^o are obtained from the solution of this problem with closed lateral boundaries, that is, subjected to an undrained condition. This implies that, according to Eq. (18), $p^0 = -\alpha Q \epsilon_v^0$.

Due to the symmetry planes, only a quarter of the domain can be considered by prescribing zero normal displacements on boundaries $x = 0$ and $y = 0$, as illustrated in Fig. 3b. With the right boundary closed, when the force F is applied on the top boundary a uniform pressure p^0 establishes along the entire domain. When the right boundary is opened, the pore pressure in $x = L$ immediately drops to P_{out} and a pressure front of disturbance travels towards the interior of the domain. In Fig. 3b, the dark gray area, referred to as region B, represents the pore pressure in the interior of the slab that has not yet been affected by the pressure front. Region A, on the right side of Fig. 3b, colored in light gray, represents the area already disturbed by the pressure front. As the pressure front migrates to the interior of the slab, region A gets larger and, consequently, region B is reduced until it finally disappears when the pressure front reaches position $x = 0$.

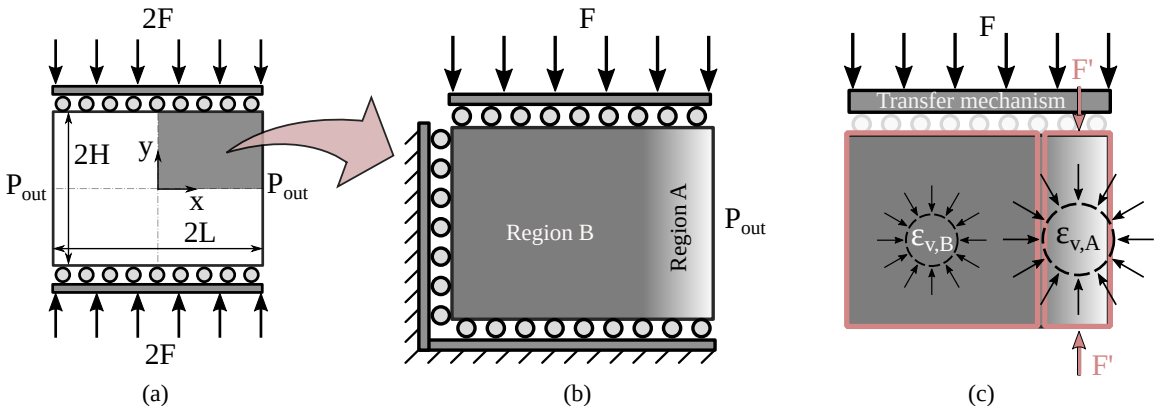

Figure 3. Boundary conditions for Mandel's problem.

As long as region B still exists, which implies that the pressure front did not fully penetrate the slab yet, the pore pressure in this region increases above the initial pressure p^0. This pressure increase is precisely the Mandel-Cryer effect. In order to understand the reasons for this effect to appear we have to first recall that wherever there is a pressure decrease due to fluid loss, the porous material tends to shrink. This is exactly what happens in region A, where the pressure values are lower than p^0, as represented in light gray. Due to the boundary conditions imposed, region A can freely deform in the horizontal direction, but not in the vertical direction. The vertical movement is restricted at the bottom boundary, and the top boundary will only move in the vertical direction if the entire top boundary moves as well, according to the boundary condition of Eq. (19). Therefore, when region A shrinks it will necessarily pull down the top boundary with a force F', as represented in Fig. 3c. The additional compressive force F' is transferred to region B through the top boundary, since it has to satisfy Eq. (19). This means that region B will be forced to shrink a little bit further (beyond the volumetric strain caused by force F), thus forcing the pore pressure to increase.

From the discussion above, it should be clear that the boundary condition imposed at the top boundary, enforcing equal vertical displacement according to Eq. (19), is the mechanism responsible for transferring the volumetric strain produced in region A to region B. It is also interesting to notice that the force F' should increase as the pressure front penetrates the slab, because the shrinking region (region A) gets larger. Furthermore, the velocity in which the pressure disturbance travels is controlled by the time integral in Equations Eqs. (16) and (17). Hence, when the pressure front reaches the center of the

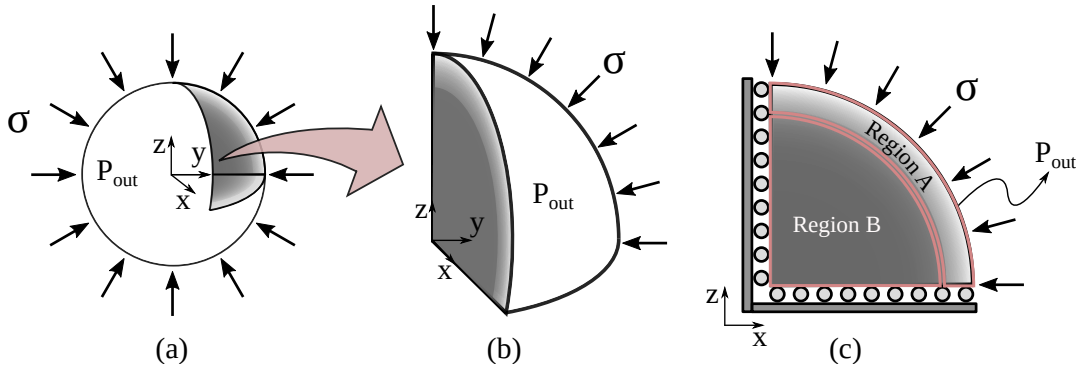

Figure 4. Boundary conditions for Cryer's sphere problem.

slab, Eq. (16) predicts that the pore pressure increase starts to dissipate due to the fluid movement, even though the solid matrix is still undergoing a compressive deformation, and the force F' starts to decrease until it completely vanishes.

Cryer's sphere

This problem refers to a poroelastic sphere of radius R fully saturated with a slightly compressible fluid. A normal stress σ is applied on the entire surface of the sphere, which is also fully permeable with prescribed pressure P_{out}, as depicted in Fig. 4a. Initially, the normal stress is applied under undrained condition (impermeable surface) and the resulting pore pressure and volumetric strain fields (p^0 and ϵ_v^0, respectively) satisfy Eq. (18). Due to the symmetry planes of the problem, only one eighth of the sphere can be considered, as represented in Fig. 4b. In this simplified domain, zero normal displacements are prescribed on the flat surfaces.

When the boundary of the sphere is opened to fluid flow at $t = 0$, a pressure front travels towards the center of the sphere. The pressure front defines the region A in Fig. 4c, which is actually the crust of the sphere. The core of the sphere that has not yet been reached by the pressure front defines the region B. The interesting behavior in this problem is observed in the center of the sphere, where the pore pressure raises above the initial pressure p^0 during the time the pressure front takes to reach this position. Although this is exactly the same Mandel-Cryer effect as observed in Mandel's problem, in this case the transfer mechanism of the volumetric strain is different and it is discussed below.

According to Eq. (16), wherever there is fluid loss, the porous matrix tends to shrink. In the sphere of Fig. 4, region A undergoes a fluid loss, since it is in contact with the surface with prescrebed pressure P_{out} (notice that $P_{\text{out}} < p^0$), and consequently the entire crust of the sphere tends to shrink. Now we turn our attention to what happens with the inner surface of region A as it shrinks. If the area of this inner surface is reduced, then the crust will compress the core (region B) of the sphere. In order analyze the behavior of the inner surface of region A, we can make use of the similarities between poroelasticity and termoelasticity and see what happens with a hole in a material undergoing a thermal contraction. Let us consider, for example, a plate at temperature T_0 with a hole of diameter D_0 at the center, as represented in Fig. 5. If the temperature is reduced to T_1, then the diameter of the hole will be reduced to D_1 and so the area of its inner surface. By analogy, this is exactly what happens with the crust of the sphere, that is, the area its inner surface tends to be reduced, thus compressing the core of the sphere. It is interesting to notice that the more the pressure front approaches the center of the sphere and region A gets thicker, the more compressed will be the region B.

The paragraph above just described the transfer mechanism of volumetric strain mentioned in Subsection 3.2 as a fundamental ingredient for the Mandel-Cryer effect to be observed. The transfer mechanism in Cryer's sphere, therefore, can be summarized as follows: as the crust tends to shrink it compresses the core of the sphere, thus increasing its pore pressure. Only when the pressure front reaches the center of the sphere the pore pressure starts to dissipate, since the time integral of Eq. 16 begins to play its role. It is important to emphasize that the entire sphere will be compressed anyways due to the normal

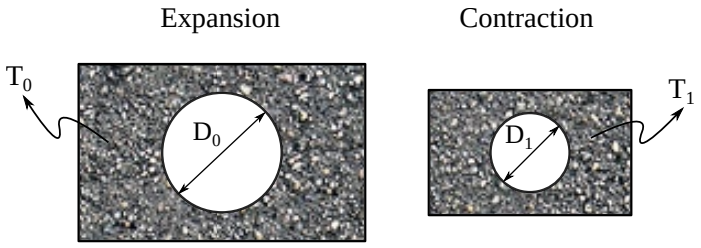

Figure 5. Thermal expansion of a flat plate with a circular hole.

stress σ prescribed on its surface. However, the contraction of the crust produces an additional compression that promotes the pressure increase above p^0. In fact, if this hypothesis is valid, the Mandel-Cryer effect should be observed even in the absence of the normal stress σ, since the transfer mechanism is independent of it. This situation is tested in the results section.

4 Poroelastic column

In this section we provide a physical interpretation for the vertical displacement profile resulted from a poroelastic column, with sealed boundaries, under the influence of the gravitational field (hereafter, this case is referred to as problem III). In order to explain why the resulting displacement profile for this problem defies our intuition we first discuss two similar problems that people usually feel more comfortable with. These two auxiliary problems are referred to as problems I and II. We show that the physical insights provided by these two problems leads our intuition to take wrong conclusions about the physical behavior of problem III. In the subsections below, these three problems are discussed.

4.1 Problem I

When implementing a numerical scheme for solving linear elasticity or poroelasticity, one of the first problems to be solved is a unidimensional column subjected to oedometric condition in the absence of body forces, such as the gravitational field. A compressive load is usually applied on the top boundary, which can freely move in the vertical direction. For a poroelasticity model, fluid flow is not allowed through any boundary of the domain, which characterizes an undrained consolidation. This situation is illustrated in Fig. 6a. Whether it is linear elasticity or poroelasticity, the resulting vertical displacement w linearly ranges from zero at the bottom of the column, due to the prescribed boundary condition, to its

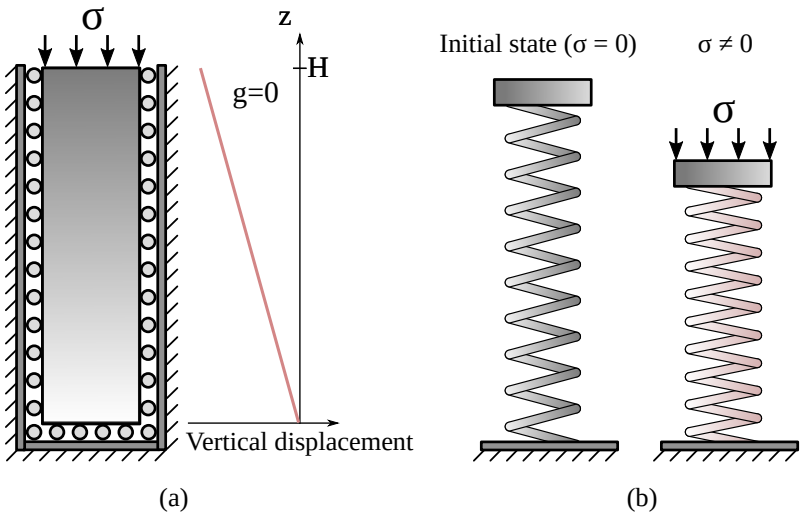

Figure 6. (a) An elastic or poroelastic material subjected to compressive load and without gravity. (b) Spring-mass system. Obs: the red color means the spring is compressed.

maximum value at the top boundary. The volumetric strain can be obtained by taking the derivative of w along the z direction, which is always constant in this case, thus every point of the column is equally deformed. It should not be difficult to wrap our minds around this result since the column actually behaves as a simple mechanical spring, as illustrated in Fig. 6b.

4.2 Problem II

Problem II defies our minds a little bit more. It refers to an elastic material under the influence of a gravitational field, as depicted in Fig. 7a. In the absence of a compressive load at the top boundary, the resulting displacement profile still presents its maximum value at the top boundary but the maximum volumetric strain is at the bottom of the column. This is because the bottom layer carries all the weight of the column above, while the top boundary does not carry any weight at all and therefore it does not experience any deformation, which can be seen by recognizing that $\partial w/\partial z$ equals zero at this position. In fact, the weight carried by each layer of material linearly decreases from the bottom (maximum) to the top of the column (zero). This fact requires that the volumetric strain profile has to be linear. The analytical solution of the equilibrium equations can be easily obtained for this problem by simple integration and it provides, indeed, the quadratic profile represented in Fig. 7a for the vertical displacement. The important thing to observe is that, just like in the previous problem, described in Fig. 6, the maximum displacement is still on the top boundary and every point of the column undergoes a negative volumetric strain (compression).

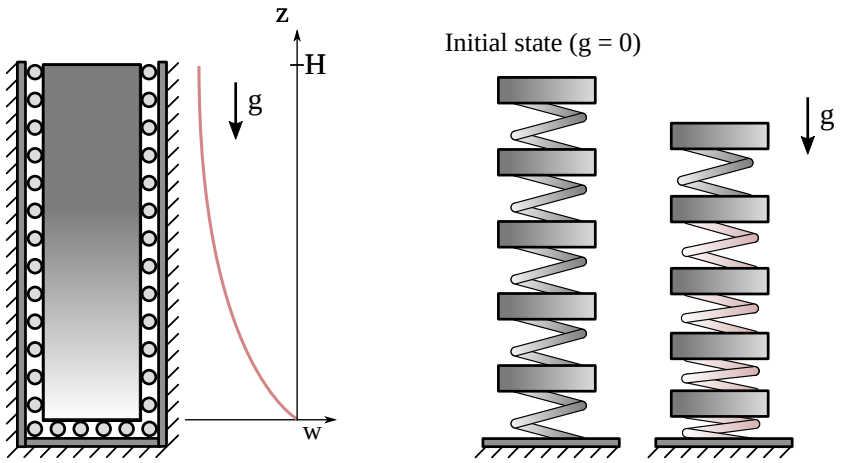

Figure 7. (a) Elastic material under the influence of a gravitational field. (b) Spring-mass system. Obs: the red, gray and blue springs denote springs under compression, undeformed and under traction, respectively.

This problem can be roughly modeled by a stack of blocks with mass m connected by springs with stiffness K, as represented in Fig. 7b. It is clear that the spring on the bottom carries the weight of all five blocks, while the top one only holds the upper block. As a consequence, all springs are under compression, specially the one at the bottom. Additionally, the upper block is the one who displaces the most since it comprises the upper spring deformation and the displacements of each block bellow.

If an external compressive load is applied on the top boundary, as in problem I, we still observe a maximum compression at the bottom of the column and a maximum displacement at the top boundary, as shown in Fig. 8a. In this case, however, it is important to observe that the top boundary is not undeformed anymore, since $\partial w/\partial z$ is not zero at this position. The reason for this is, although the top boundary does not carry any weight, it is subjected to an external load σ that forces it to be compressed. The corresponding spring-mass system for this case is depicted in Fig. 8b.

These simple mass-spring systems, therefore, properly reproduce the physical behavior of the original problem. This simplified model will turn to be very helpful to understand the physics of problem III,

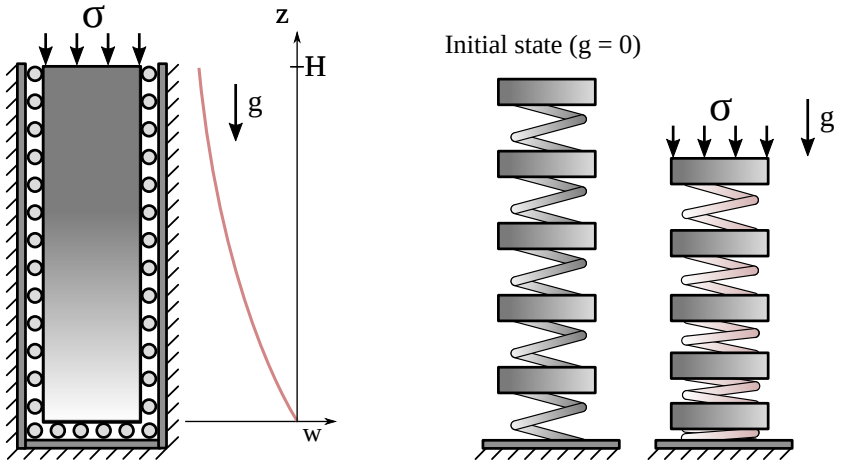

(a) (b)

Figure 8. (a) Elastic material under the influence of a gravitational field and a compressive load. (b) Spring-mass system. Obs: the red, gray and blue springs denote springs under compression, undeformed and under traction, respectively.

presented in the sequence.

4.3 Problem III

In this case, a permeable porous material saturated with a slightly compressible fluid is subjected to the same boundary conditions of the previous problem II. According to Terzaghi's principle of effective stress, both solid and fluid phases support the total weight of the system (remember that there is no external load applied). In this manner, we could think of this system as a solid material with mechanical properties resulting from a combination of the mechanical properties of both solid and fluid phases. The mechanical properties of the solid phase can be defined, in this case, by the constrained modulus $M = \lambda + 2G$. The fluid phase, since it only produces normal stresses, can be characterized by the fluid compressibility, c_f. Evidently, the inverse of the fluid compressibility gives an idea of "fluid stiffness". This interpretation suggests that this problem is similar to problem II and it can also be modeled by a system of springs and masses. In this case, however, between two blocks there are two springs, one representing the solid stiffness (K_s) and the other representing the fluid stiffness (K_f), as illustrated in Fig. 9. From this interpretation, we should expect the vertical displacement profile to behave just like

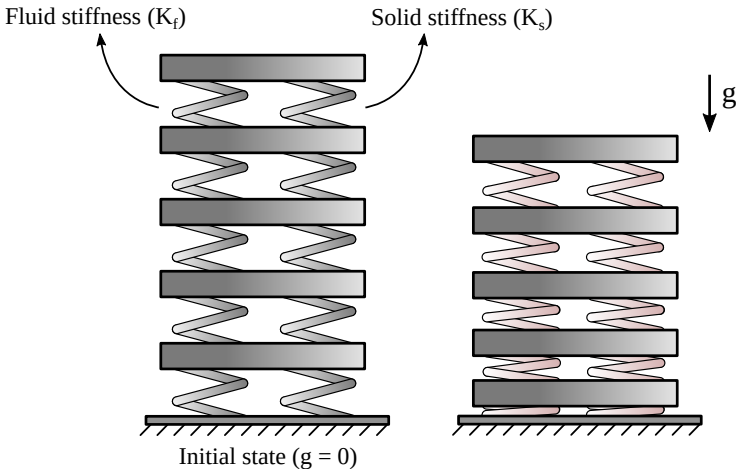

Figure 9. Hypothetical spring-mass system for problem III. Obs: the red, gray and blue springs denote springs under compression, undeformed and under traction, respectively.

as in problem II, that is, the maximum displacement should be at the top boundary and the maximum compression at the bottom of the column, as in Fig. 7a. With this idea in mind, a very unpleasant feeling appears when we numerically solve this problem and come across a displacement profile like the one shown in Fig. 10a. From the point of view we built based on the previous problem II, there would be no reasonable explanation to observe, for instance, a maximum displacement anywhere else other than the top boundary. Even worse, what could possibly be the reason to justify a region of the domain to undergo an expansion such as the one we see close to the top boundary? The conclusion is unavoidable: the assumption of a material with combined mechanical properties does not apply. We now present an alternative hypothesis for explaining this behavior.

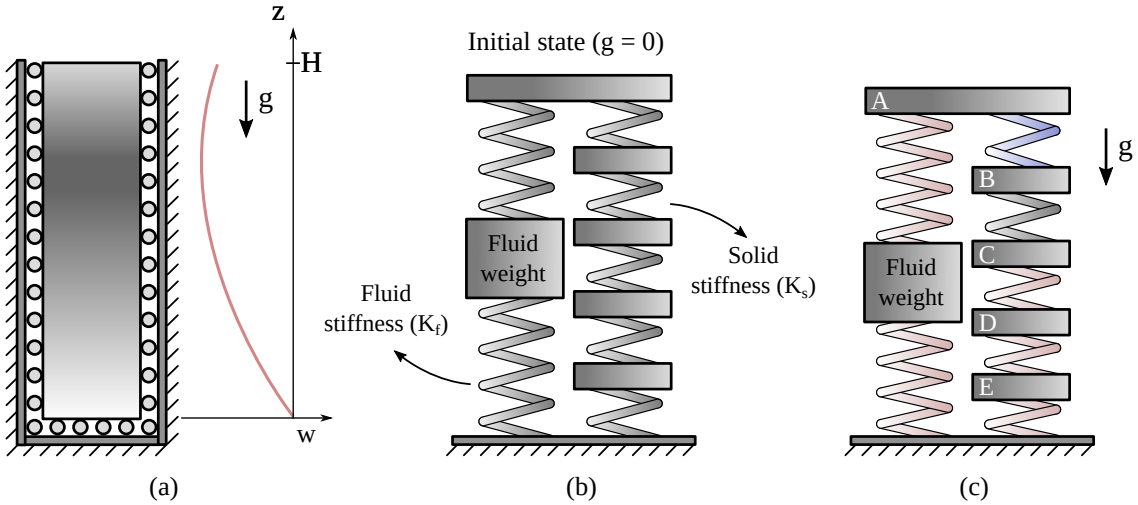

Figure 10. (a) Poroelastic material under the influence of a gravitational field. (b) Spring-mass system. Obs: the red, gray and blue springs denote springs under compression, undeformed and under traction, respectively.

The hypothesis just presented in the previous paragraph actually holds true for a porous material with zero permeability, which means that the pore spaces are not connected to each other. In this case, because the fluid is trapped between the different layers, each layer of the column is carried by the solid stiffness and the pore pressure of the fluid, so the spring-mass system represented in Fig. 9 is correct. However, as mentioned in the beginning of this subsection, problem III actually refers to a permeable material, which means that the fluid is not trapped in a single pore of the domain, but instead, it can freely move inside the poroelastic column. As a consequence, the fluid is not able hold each layer of the domain anymore because a relative motion between the solid and fluid phases is perfectly allowed. In other words, when the middle layers of the poroelastic column start to move, they do not face any resistance from the fluid phase. Obviously, this is not the case for the top and bottom boundaries due to the undrained condition. In these two layers (top boundary and bottom boundary), the relative velocity between the solid and fluid phases is zero, which means that they are the only layers that feel the resistance of the fluid. This is equivalent to have a long spring connecting the bottom to the top boundary in such a way that whenever these two boundaries come closer to each other the spring tends do push them in opposite directions. So a proper spring-mass system could be the one represented is Fig. 10b. On the left side of Fig. 10b it is represented the fluid phase, where the springs represent the fluid stiffness (K_f) and the block represent the fluid weight, given that $\rho_f \neq 0$.

It is possible to show that the spring-mass system presented in Fig. 10b does reproduce the behavior shown in Fig. 10a. For convenience, the springs corresponding to the solid and fluid phases are referred to as springs *S* and *F*, respectively. Now, let us consider an almost incompressible fluid ($c_f \to 0$) and a soft porous material, such that there is a large difference between the stiffnesses of springs *F* and *S*, that is, $K_f >> K_s$. This means that, under the same external load, spring *F* deforms way less than spring *S*. In this manner, when the gravitational field is turned on, the spring *F* deforms very little and thus the displacement of the top boundary (block A in Fig. 10c) is very small as well. It is easy to see in Fig.

10c that the displacement of block B equals the displacement of block A plus the deformation the upper spring *S*. Since K_s is very small, the upper spring *S* will surely undergo significant deformation, which implies that the displacement of block B is larger than the displacement of block A. In other words, the spring *S* connecting blocks A and B is necessarily under traction, which means that the solid phase has to expand close to the top boundary, as observed in the displacement profile presented in Fig. 10a. If we now look at the lower spring *S*, we see that it will only expand if block E moves upwards, which has no reason what so ever to happen, so it will certainly be compressed. The same idea applies to the other springs. Eventually, there can be a situation in which two neighbor blocks have the same displacements, such as blocks B and C, and thus the spring connecting them is undeformed. This situation is equivalent to have a $\partial w/\partial z = 0$, as observed in the vertical displacement profile of Fig. 10a. It is also important to emphasize that the block representing the fluid weight in Fig. 10c is only sustained by the lower spring F. Therefore, the hypothesis for explaining problem III is that the fluid filling the pore channels actually holds the top boundary in position, while the gravitational field pulls down the layers in the middle section of the poroelastic column, thus causing a maximum displacement somewhere below the top boundary.

According to the hypothesis drawn above, if the fluid phase is very compressible such as $K_f << K_s$, then the lower spring F is not able to sustain the fluid weight without the help of the upper spring F. Thus the upper spring F must be under traction, as represented in Fig. 11a. As a consequence, the top boundary perceives a load applied downwards due to the fluid weight. In this manner, the problem is similar to the one represented in Fig. 8, where a solid material is subjected to the gravitational field and a compressive external load.

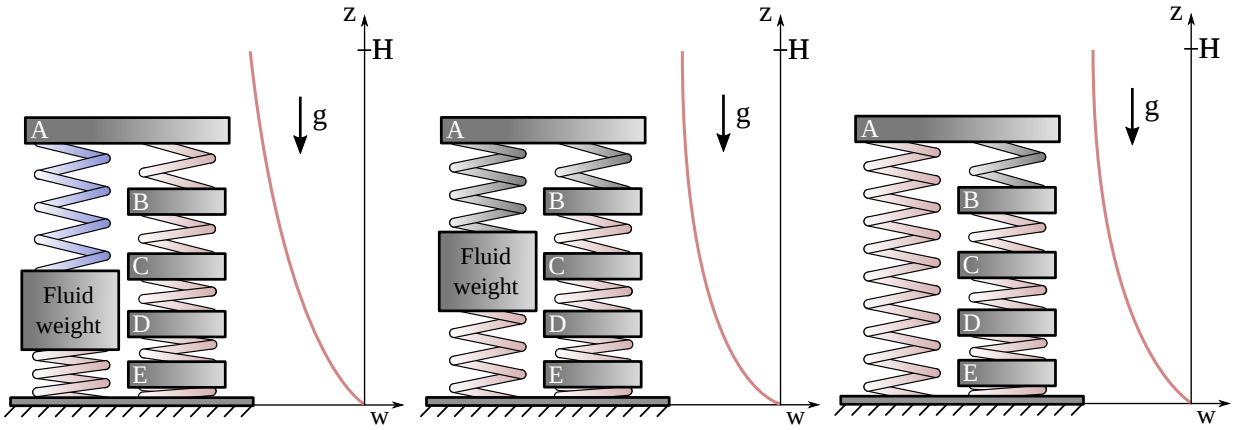

(a) $K_f << K_s$ (b) $K_f < K_s$ (c) $\rho_f = 0$

Figure 11. (a) Very compressible fluid. (b) Fluid with a specific compressibility. (c) Weightless fluid phase. Obs: the red, gray and blue springs denote springs under compression, undeformed and under traction, respectively.

If we slowly reduce the fluid compressibility, that is, increase K_f, there will be a point where the lower spring F will completely sustain the fluid weight without compressing the upper spring F, as depicted in Fig. 11b. At this point, the top boundary does not feel the presence of the fluid phase and the problem reduces to problem II with no external load applied, as presented in Fig. 7. Another way of reproducing the displacement profile of problem II with no external load, is to consider a very compressibility c_f, such that $K_f << K_s$, and to consider a weightless fluid ($\rho_f = 0$), as represented in Fig. 11c. In this case, the spring F, representing the fluid phase, does not offer any resistance to the top boundary, which means that the solid phase does not perceive the presence of the fluid. Therefore, the porous matrix behaves as a completely solid material.

5 Numerical Formulation

In the previous sections, the Mandel-Cryer effect and the poroelastic column under the gravitational field have been discussed and a few hypotheses have been raised in an attempt to explain these phenomena. In order to prove these hypotheses, the situations previously described are reproduced through numerical experiments and the governing equations of Biot's consolidation model are numerically solved. The numerical formulation is briefly described in this section.

5.1 Element-based Finite Volume Method (EbFVM)

Traditionally, the finite element method (FEM) is the most common technique employed for obtaining the discretized equations in coupled poroelasticity. In this paper, however, we employ the element based finite volume method (EbFVM), which combines important features from both FEM and FVM. This method is naturally applied to unstructured grids that can be composed of different types of elements, which provides great geometrical flexibility for representing complex domains. In order to handle these unstructured grids, the EbFVM uses the element shape functions and their derivatives in a similar way to the finite element method. Finally, as a finite volume method the EbFVM ensures local conservation, which is an important feature specially for fluid flow problems.

The most important entity in any version of the finite volume method is the control volume, where the property balance is performed. In the EbFVM, each element of the grid is subdivided into subelements (or sub-control volumes) associated to each element vertex. In this manner, the control volume Ω_i is built by the union of all sub-control volumes sharing the same grid node i, as illustrated in Fig. 12. Moreover, every control volume Ω_i is bounded by a control surface Γ_i that can be further split into a set of faces. Each face of the control volume contains an integration point ip and an area vector $\mathbf{s}$ point outwards the control volume.

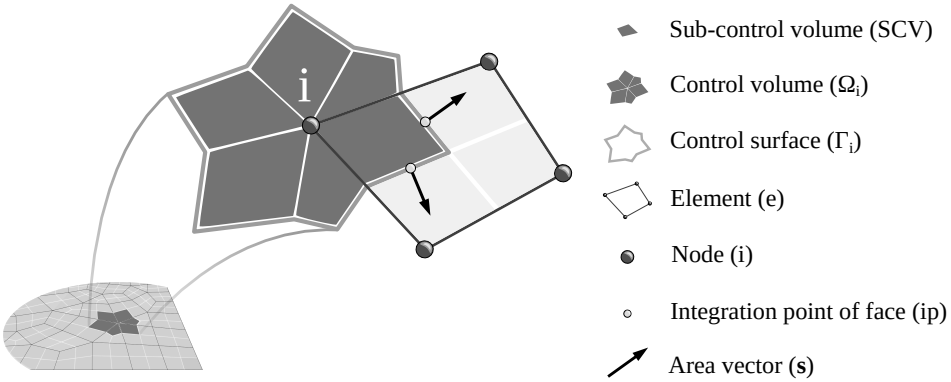

Figure 12. Control volume construction and geometrical entities.

The discretized mass conservation e stress equilibrium equations are obtained by first integrating Equations 1 and 6 on a control volume Ω_i. The volumetric integrals of the divergence terms are transformed into surface integrals by the divergence theorem. Next, the midpoint rule is applied to evaluate the integrands (fluxes) at the integration points surrounding the control volume. The element shape functions and their derivatives are then used for approximating these fluxes at the integration points. Finally, the mass conservation equation (Eq. 6) requires a time integration for evaluating the accumulation terms. In this work we use a fully implicit first-order backward Euler scheme. A detailed description of the discretization process can be found in Honório et al. [13]. This procedure leads to the algebraic representation of the mass balance and the stress equilibrium equations, which can be respectively written as,

$$\frac{\Delta\Omega_i}{Q\Delta t}p_i + \sum_{ip\in\Gamma_i}(E_{ip}\mathbf{u}^e - H_{ip}\mathbf{p}^e) = \frac{\Delta\Omega_i}{Q\Delta t}p_i^o + \sum_{ip\in\Gamma_i}(E_{ip}\mathbf{u}^e)^o + b^p, \tag{20}$$

$$\sum_{ip \in \Gamma_i} (K_{ip}\mathbf{u}^e - L_{ip}\mathbf{p}^e) = b_i^u \Omega_i, \tag{21}$$

where $\mathbf{p}^e$ and $\mathbf{u}^e$ respectively denote the pressure and displacement values associated to the element e that contains the current integration point ip of the summation. Terms $K_{ip}\mathbf{u}^e$ and $L_{ip}\mathbf{p}^e$ in Eq. 21 represent the forces acting on the surface Γ_i due to the effective stress tensor and to the pore pressure, respectively. In Eq. 20 the terms $E_{ip}\mathbf{u}^e$ and $H_{ip}\mathbf{p}^e$ respectively represent the volumetric strain and the mass fluxes due to Darcy's law. Additionally, the superscript "^{o}" in Eq. 20 is used to denote the variables evaluated at the previous time step t, and no superscript is used for the current time level $t + \Delta t$.

When the procedure described above is performed for each control volume of the grid, the resulting set of equations can be grouped in a single system of equations with the following form,

$$\begin{bmatrix} -\mathrm{K} & \mathrm{L} \\ \mathrm{E} & \mathrm{A} - \mathrm{H} \end{bmatrix} \begin{bmatrix} \mathbf{u} \\ \mathbf{p} \end{bmatrix} = \begin{bmatrix} \mathbf{b}^u \\ \mathbf{b}^p \end{bmatrix}, \tag{22}$$

where matrix A represents the accumulation terms, H represents the mass fluxes due to the seepage velocity, Q express the mass fluxes due to the solid movement (volumetric strain), and K and L represents the effective stresses and the pore pressures acting on control volume's surfaces, respectively. Finally, vectors $\mathbf{b}^u$ and $\mathbf{b}^p$ are the right-hand side of stress equilibrium and mass conservation equations. In this work, the linear system represented in Eq. 22 is solved with a fully implicit scheme by an LU decomposition.

6 Results

The purpose of this section is to present a systematic sequence of problems that allows to test the hypotheses raised in this paper. Firstly, we verify the correction implementation of the governing equations of coupled poroelasticity. The numerical solutions are compared with the analytical solutions for the Mandel's problem and the Cryer's sphere. On the implementation is verified, we setup a few different problems to reproduce the Mandel-Cryer effect and test the hypothesis of the transfer mechanism discussed in Subsection 3.2. In the sequence, the poroelastic column subjected to the gravitational field is addressed. The different scenarios discussed in Subsection 4.3 are reproduced by adjusting the poromechanical properties.

6.1 Verification of the numerical formulation

In this paper we employ numerical simulations as a tool for testing the hypotheses discussed in Sections 3 and 4. Therefore, it is of utmost importance to verify the correct implementation of the numerical formulation presented in Section 5. For this purpose, we perform simulations for the Mandel's problem and the Cryer's sphere and compare the numerical results with the analytical solutions available, which can be found in Verruijt [14]. For both problems, the poromechanical properties used are summarized in Table 1. The fluid properties are $c_f = 3,0303 \times 10^{-10}$ Pa^{-1} and $\mu = 1,0 \times 10^{-3}$ Pa.s.

Mandel's problem

The boundary conditions for Mandel's problem are presented in Subsection 3.2. Since we employ a three-dimensional formulation, the geometry for this problem is a cube of 1 meter edges and the grid employed is composed of 20.860 tetrahedra and 4.614 nodes, as illustrated in Fig. 13a. Normal displacements are set to zero at the bottom boundary ($z = 0$), at the left boundary ($y = 0$) and at the front ($x = 0$) and back ($x = -1$) boundaries. The right boundary ($y = 1$) is traction-free and pressure is prescribed to be zero (fully drained). The top boundary ($z = 1$) is subjected to a total force $F = -10.000$ kN and the vertical displacement is not allowed to vary in the $x - y$ plane.

Table 1. Poromechanical properties for verification problems.

Property	Nomenclature	Value
Biot's coefficient	α	0,978
Porosity	ϕ	0,19
Poisson's ratio	ν	0,2
Shear modulus	G	0,6 GPa
Solid compressibility	c_s	$2,78 \times 10^{-11}$ Pa^{-1}
Permeability	k	$1,9 \times 10^{-12}$ m^2

Figure 13b shows good agreement between the analytical and numerical solutions of the pressure profiles along the horizontal direction for different time levels. It is important to notice the pressure increase at position $y = 0$ until $t = 0,02$ s. This is precisely the Mandel-Cryer effect caused by contraction of the right boundary.

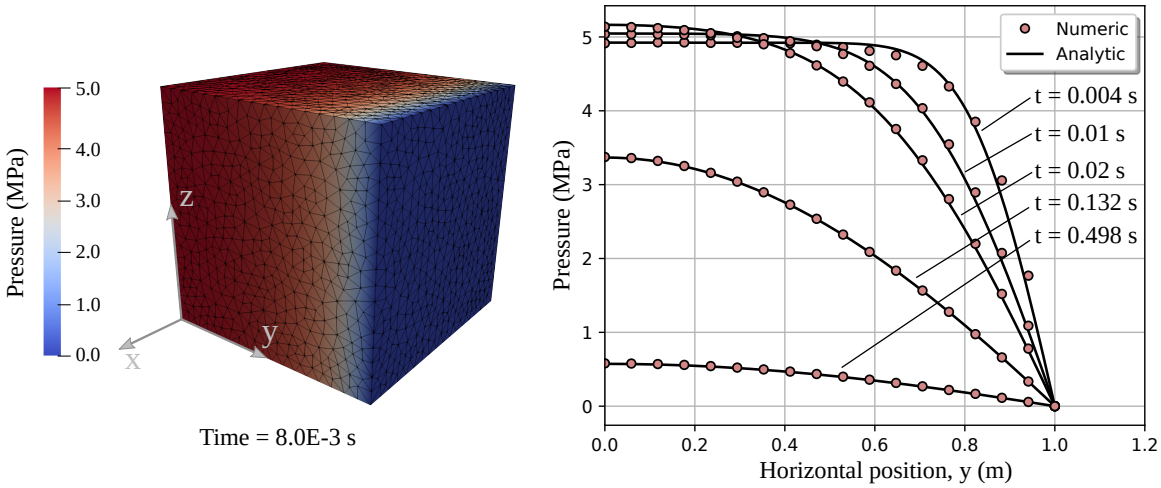

(a) (b)

Figure 13. (a) Tetrahedral grid and pressure field. (b) Pressure profiles along horizontal direction for different time levels.

Cryer's sphere

For the Cryer's sphere, only an eighth of a sphere with 1 m radius is simulated, as depicted in Fig. 14a. The grid employed is composed of 17.370 tetrahedra and 3.928 nodes. In this problem, zero normal displacements and undrained condition are prescribed over the flat surfaces. On the outer surface, pressure is prescribed to be zero and a compressive load of 10 kPa is applied. The analytical solution for this problem provides the pressure behavior at the center of the sphere. In Fig. 14b, the analytical and numerical solution of the pressure at the center of the sphere is plotted against time. As shown in this figure, the pressure increase during the begin of the simulation, which characterizes the Mandel-Cryer effect, is perfectly captured by the coupled numerical formulation. It is also interesting to notice in Fig. 14a that the region swept by the pressure front (referred to as region A in Fig. 4c) can be clearly identified. We suggest that it is precisely the shrinkage of this region what causes the core of the sphere to compress even more, thus causing the pressure to increase above the initial level.

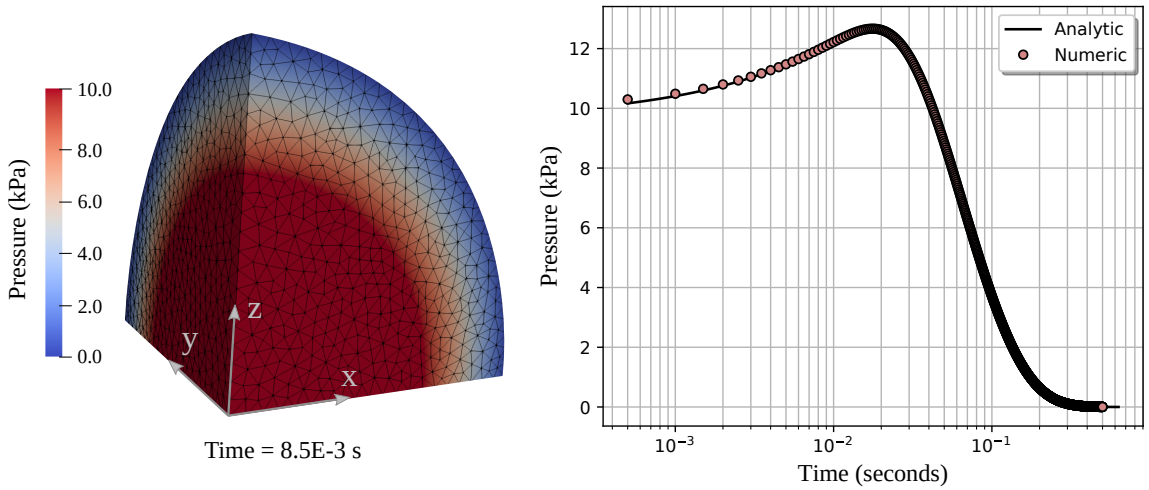

(a) (b)

Figure 14. (a) Tetrahedral grid and pressure field. (b) Pressure at the center of the sphere along time.

6.2 Numerical experiments: Mandel-Cryer effect

According to the hypothesis developed in Section 3, the additional pressure increase that characterizes the Mandel-Cryer effect occurs because of a sort of mechanism that transfers the volumetric strain from on region of the domain to another another region. This hypothesis implies that the Mandel-Cryer effect has nothing to do with the external load applied. Therefore, one of the strategies for testing this hypothesis is to solve the Mandel's problem and the Cryer sphere with no external load applied. In this case, the initial pressure can be set to zero, so the porous matrix expanded at the beginning of the simulation. Finally, a negative pressure is prescribed along the draining boundary in order to cause it to shrink and thus inducing the Mandel-Cryer effect. This strategy is employed in both problems presented below.

Mandel's problem

As mentioned above, no external load is applied to the Mandel's problem. At the draining boundary, a prescribed pressure of -10 kPa is applied. In this case, a pressure increase at the center of the slab necessarily means it is under compression. If there is no compressive load at the top boundary, then there must be another cause. As we can see in Fig. 15, the pressure at the center of the slab does increase as the pressure front penetrates the domain. As expected, only when the pressure front reaches the center of the domain the pore pressure starts to alleviate. The correlation between the pressure increase and the pressure front (region A in Fig. 19) suggests that the Mandel-Cryer effect is indeed caused by the volumetric strain transferring mechanism, which in this case is the horizontal orientation imposed on the top boundary.

Cryer's sphere

In Section 3 we also raised an argument that the pressure at the center of the sphere increases as the crust (region A in Fig. 4c) gets thicker. Once the pressure front reaches the center of the sphere, then the fluid starts to flow due to the pressure gradient and thus the pore pressure starts to dissipate. In fact, the fluid flow, represented by the time integral on the right hand side of Eq. 16, is the only reason for the pressure decrease. If the core of the sphere is impermeable, for example, then the fluid is not able to move and thus there will be no pressure decrease unless the center of the sphere expands. In other words, if the pore pressure at the center of the sphere, which is impermeable, does not decay it means it is constantly under compression. If there is no external load applied to the sphere, then the only reason for the core to be compressed is that the crust must be compressing it. The hypothesis here is that this compression is caused by the shrinkage of the crust.

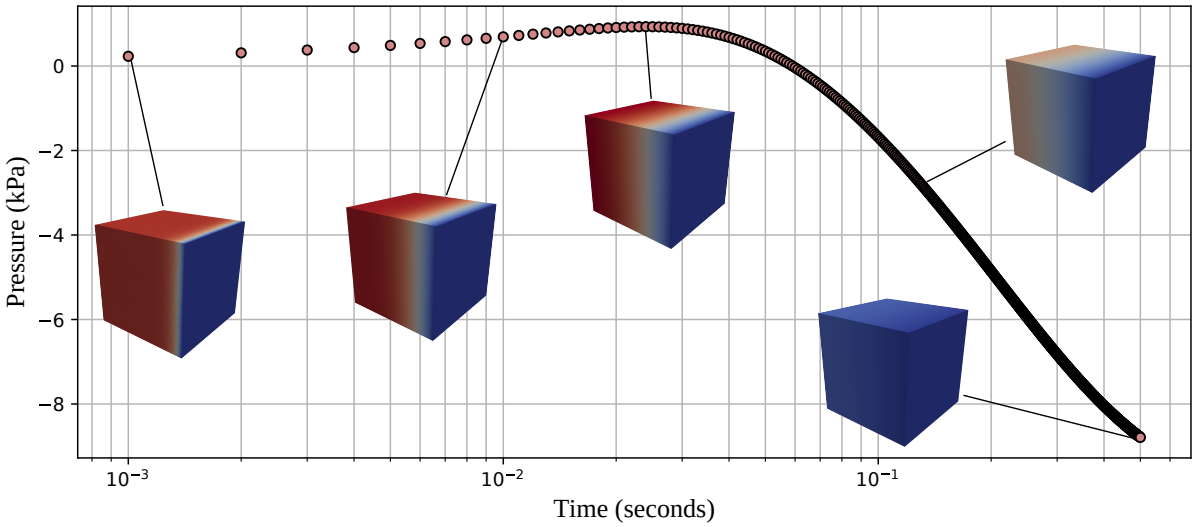

Figure 15. Pore pressure at the center of the slab ($x = y = z = 0$).

The Cryer's sphere is now solved with no external load, zero initial pressure and a pressure of -10 kPa prescribed on the external surface. Additionally, the sphere has 1 m radius and it is composed of two concentric regions. The interface between the two regions is at $R = 0,5$ m. The poromechanical properties of both regions are summarized in Table 1, except for the inner region, which has zero permeability. Figure 16 shows the pressure behavior at the center of the sphere, as well as the pressure distribution at certain time levels. As predicted in the previous paragraph, the pressure at the center of the sphere increases until certain level and does not give any indication that it is going to decrease. This confirms our hypothesis that the pressure increase does not have anything to do with the external load and the core of the sphere is permanently under compression.

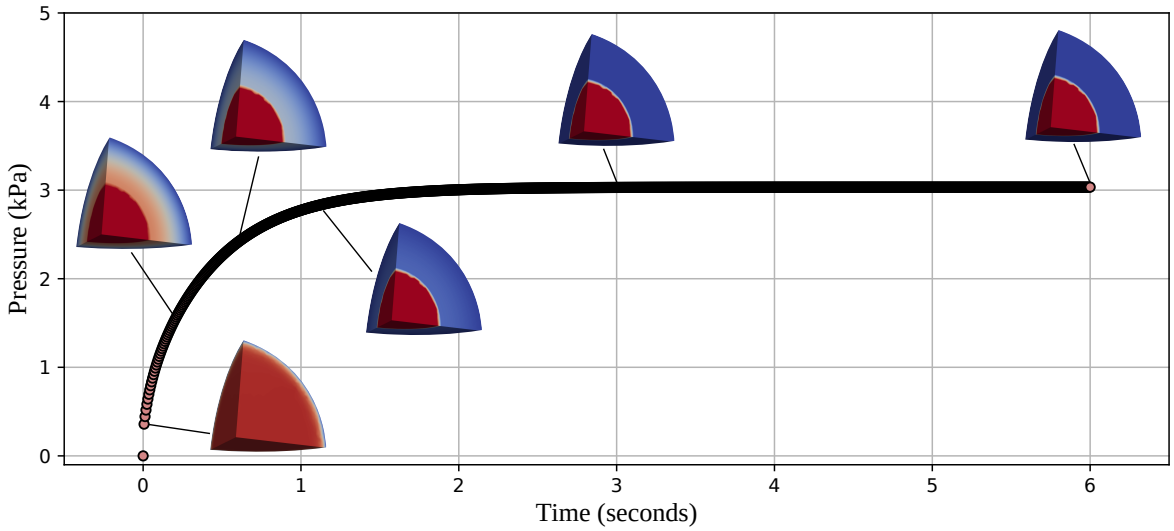

Figure 16. Pore pressure at the center of a sphere with impermeable core.

6.3 Numerical experiments: Poroelastic column

The poroelastic column discussed in Section 4 is solved with a 6 meters high column and a 1×1 meters base. The vertical boundaries are prevented from normal displacement, the bottom boundary is fixed and the top boundary is traction-free. All boundaries are impermeable and the gravitational acceleration is $9,81$ m/s^2. The poromechanical properties of the solid matrix are those presented in Table

1, with two exceptions: $c_s = 0,0$ and $\alpha = 1,0$. Additionally, the solid and fluid densities are $\rho_s = 2.700$ kg/m^3 and $\rho_f = 1.000$ kg/m^3, respectively. Different from the previous subsection, where the pressure field has been analyzed, in this subsection only the vertical displacement profiles are presented. The resulting pressure for this problem is always the expected hydrostatic profile, so they are not of interest in this paper.

In the examples presented below we intend to reproduce the behaviors illustrated in Figures 10 and 11. This will be achieved by simply changing the fluid compressibility, c_f, which is equivalent to modify the stiffness of the springs representing the fluid phase in the spring-mass systems discussed in Section 4. By setting the fluid compressibility to $3,0303 \times 10^{-10}$ Pa^{-1}, for instance, the resulting vertical displacement profile is the one shown in Fig. 17a. As it can be verified, this value of c_f reproduce the behavior of a very stiff spring that holds the top boundary. In this manner, the maximum displacement is not on the top boundary, but somewhere near the middle of the column (around $z = 3,5$ meters) instead. Furthermore, it should be pointed out that most of the upper half section of the column is actually under traction, since it is indeed hanging by the top boundary. It is also important to remark that this effect would never happen if the lateral boundaries were free to move.

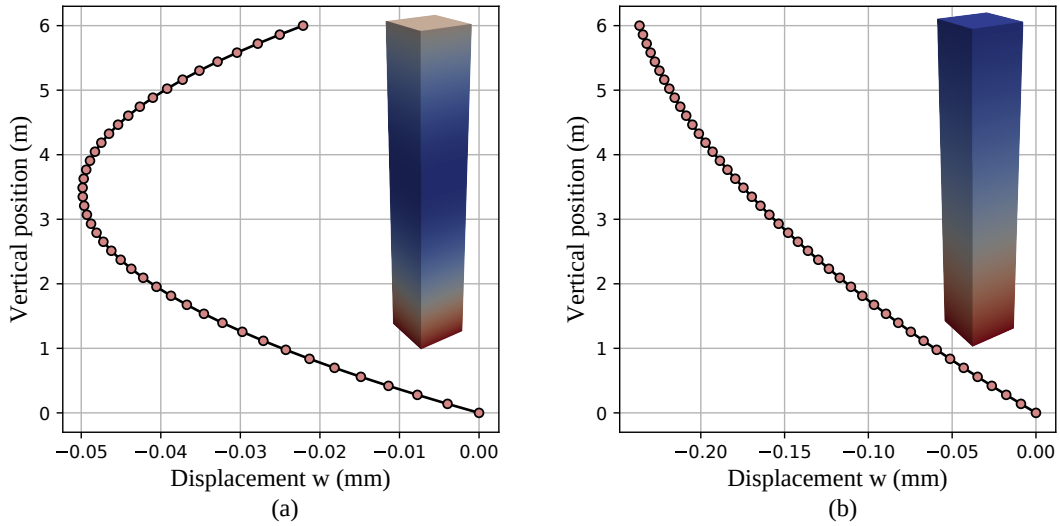

Figure 17. Displacement profiles for fluid compressibilities equal to (a) $3,0303 \times 10^{-10}$ Pa^{-1} and (b) $3,0303 \times 10^{-8}$ Pa^{-1}.

Now, by reducing the fluid compressibility to $c_f = 3.0303 \times 10^{-8}$ Pa^{-1} the situation depicted in Fig. 11a is reproduced, as it shown by the vertical displacement profile shown in Fig. 17b. In this case, the maximum displacement is indeed at the top boundary, but a careful look at this position reveals that the top boundary undergoes a compression, even though there is no solid layer above it and in the absence of any external load. This means that there must be something else exerting a force on the top boundary. Since the porous column is fully saturated, there are fluid particles in contact with the top boundary. In the presence of the gravitational field, fluid phase is also compressed so those fluid particles in contact with the top boundary move downwards. Since there is no vacuum inside the poroelastic column (fully saturated), when the fluid particles move downwards, they must pull the top boundary down as well. Therefore, it is the fluid weight that exert a force on the top boundary. If this is true, then there should be no force acting on the top boundary if the fluid is weightless, which is roughly represented by the spring-mass system shown in Fig. 11c. In other words, the derivative of the vertical displacement along the vertical direction at the top boundary should be zero. Indeed, when we set $\rho_f = 0$, the vertical displacement profile obtained is the one presented in Fig. 18a, which is precisely what was predicted.

The last problem intends to reproduce the situation described in Fig. 11b. The hypothesis behind this problem is that, by setting a particular compressibility for the fluid phase, it is possible to obtain a displacement profile just like in Fig. 18a, that is, with no deformation at the top boundary. This means that the top boundary is neither sustained by the fluid phase, as in Fig. 17a, nor pulled down, as in Fig.

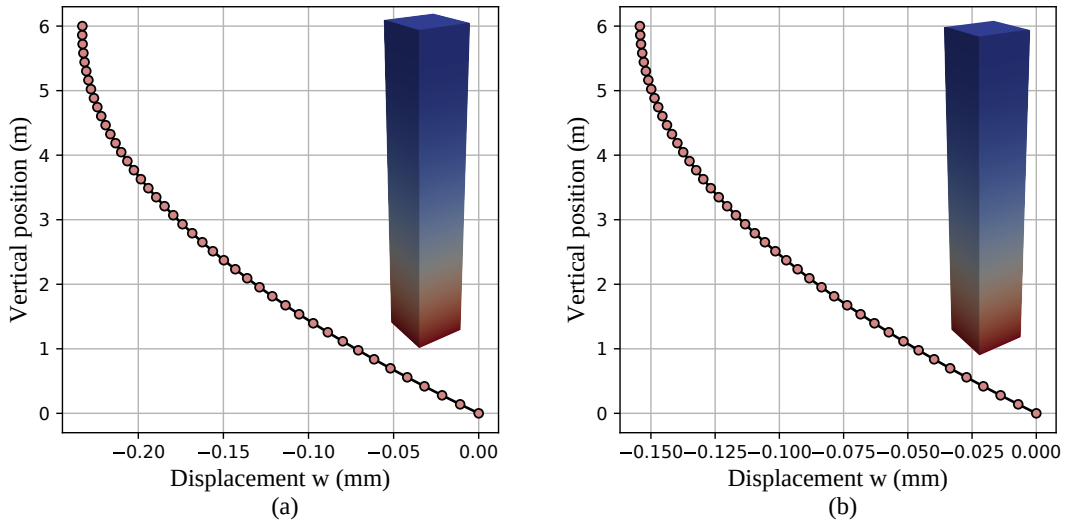

Figure 18. Displacement profiles for (a) a weightless fluid ($\rho_s = 0$) and (b) a fluid with compressibility of $4,7 \times 10^{-9}$ Pa^{-1}.

17b. For the right compressibility c_f, the solid phase and the fluid phase are both equally displaced downwards at the top boundary by the influence of the gravitational field. For the poromechanical properties used, a $c_f = 4,7 \times 10^{-9}$ Pa^{-1} produces the vertical displacement profile shown in Fig. 18b.

7 Conclusion

In this paper, a few non-intuitive behaviors that appear in coupled poroelasticity have been addressed. The equations composing Biot's consolidation model have been analyzed in order to improve our sense of the physics behind poroelasticity and to gain some insights to provide rational explanations for these counterintuitive phenomena. Numerical simulations are used in this paper as a tool for reproducing specific scenarios and to test the proposed hypotheses.

The Mandel-Cryer effect has been deeply discussed and a detailed explanation on the conditions that cause this phenomenon have been established. In fact, we suggest that the Mandel-Cryer effect can only occur when there is a mechanism that is able to instantly transfer the volumetric strain (expansion or contraction) from one region of the domain to another region. When this mechanism operates, the pore pressure is affected as well, accordingly to the mass balance equation. It has been shown that this mechanism takes different forms but it is always responsible for volumetric strain transferring. For instance, in Mandel's problem the restriction of horizontal movement of the top boundary is responsible for transferring the shrinkage close to the open boundary to the interior of the domain. For the Cryer's sphere, on the other hand, the transfer mechanism is the shrinkage of the crust of the sphere, which instantly compresses its core. According to this hypothesis, if the boundary conditions provide this transfer mechanism, then the Mandel-Cryer effect should be observed even when no external load is applied. This prediction has been precisely reproduced through the numerical experiments presented here. Additionally, although we have not addressed this problem here, we can also state that the Mandel-Cryer effect does not appear in Terzaghi's poroelastic column because the boundary conditions imposed do not create a mechanism able to instantly transfer the volumetric strain from the top boundary to the base of the column.

We have also addressed a fully saturated poroelastic column with all boundaries sealed immersed in gravitational field. Different scenarios have been described and investigated. For each one of them, a simple spring-mass system that roughly reproduce the same behavior has been presented. These spring-mass systems have proved to be very helpful in order to understand the displacement patterns that can appear when different properties are assigned to both solid and fluid phases. Once the roles played by the solid and fluid phases were well understood, a few numerical experiments have been set up to reproduce

four different situations. All numerical solutions obtained were in accordance with the behavior predicted by the spring-mass systems and reasonable physical explanations have been provided.

Although coupled consolidation is a well understood phenomenon and the model equations are well established, the sense humans have about the physics of this problem is often flawed. In order to improve the understanding of this physics, besides a careful analysis of the model equations, the numerical simulation have proved to be of great help, as it allows for a fast and reliable tests of the proposed hypotheses.

Acknowledgements

This paper has been partially supported by Petrobras within project number 5850.010924.18.9, entitled ”Malhas Tridimensionais Híbridas para a Solução do Problema Acoplado Fluxo-Geomecânica”, within ”Rede Temática GEOMEC”.

References

[1] Terzaghi, K., 1923. Die berechnug der durchlassigkeit des tones aus dem verlauf der hydromechanischen spannungserscheinungen. *Sitzungsber. Akad. Wiss.(Wien). Math.-Naturwiss. Kl., Abt. Iia*, vol. 132, pp. 125–138.

[2] Terzaghi, K., 1925. *Erdbaumechanik auf Bodenphysikalischer Grundlage*. Franz Deuticke, Leipzig.

[3] Biot, M. A., 1941. General theory of three-dimensional consolidation. *Journal of applied physics*, vol. 12, n. 2, pp. 155–164.

[4] Biot, M. A., 1955. Theory of elasticity and consolidation for a porous anisotropic solid. *Journal of applied physics*, vol. 26, n. 2, pp. 182–185.

[5] Mandel, J., 1953. Consolidation des sols (étude mathématique). *Geotechnique*, vol. 3, n. 7, pp. 287–299.

[6] Cryer, C., 1963. A comparison of the three-dimensional consolidation theories of biot and terzaghi. *The Quarterly Journal of Mechanics and Applied Mathematics*, vol. 16, n. 4, pp. 401–412.

[7] Verruijt, A., 1969. Elastic storage of aquifers. *Flow through porous media*, vol. 1, pp. 331–376.

[8] Yin, S., Dusseault, M. B., & Rothenburg, L., 2007. Analytical and numerical analysis of pressure drawdown in a poroelastic reservoir with complete overburden effect considered. *Advances in Water Resources*, vol. 30, n. 5, pp. 1160–1167.

[9] Kim, J.-M. & Parizek, R. R., 1997. Numerical simulation of the noordbergum effect resulting from groundwater pumping in a layered aquifer system. *Journal of Hydrology*, vol. 202, n. 1-4, pp. 231–243.

[10] Dean, R. H., Gai, X., Stone, C. M., Minkoff, S. E., et al., 2006. A comparison of techniques for coupling porous flow and geomechanics. *Spe Journal*, vol. 11, n. 01, pp. 132–140.

[11] Detournay, E. & Cheng, A. H.-D., 1993. 5 - fundamentals of poroelasticity. In Fairhurst, C., ed, *Analysis and Design Methods*, pp. 113 – 171. Pergamon, Oxford.

[12] Biot, M. & Willis, D., 1957. The elastic coeff cients of the theory of consolidation. *J. appl. Mech*, vol. 24, pp. 594–601.

[13] Honório, H. T., Maliska, C. R., Ferronato, M., & Janna, C., 2018. A stabilized element-based finite volume method for poroelastic problems. *Journal of Computational Physics*, vol. 364, pp. 49–72.

[14] Verruijt, A., 2013. Theory and problems of poroelasticity. *Delft University of Technology*, pp. 71.